






# Hyperfine collisional excitation of ammonia by molecular hydrogen

J. Loreau <sup>1</sup>★, A. Faure <sup>2</sup>, F. Lique <sup>3</sup>, S. Demes <sup>3</sup> and P. J. Dagdigan <sup>4</sup>

<sup>1</sup>Department of Chemistry, KU Leuven, B-3001 Heverlee, Belgium

<sup>2</sup>Univ. Grenoble Alpes, CNRS, Institut de Planétologie et d'Astrophysique de Grenoble (IPAG), UMR 5274, F-38041 Grenoble, France

<sup>3</sup>Univ. Rennes, CNRS, Institut de Physique de Rennes (IPR), UMR 6251, F-35000 Rennes, France

<sup>4</sup>Department of Chemistry, The Johns Hopkins University, Baltimore, MD 21218-2685, USA

Accepted 2023 September 28. Received 2023 September 28; in original form 2023 September 4

## ABSTRACT

Ammonia is one of the most widely observed molecules in space, and many observations are able to resolve the hyperfine structure due to the electric quadrupole moment of the nitrogen nucleus. The observed spectra often display anomalies in the satellite components of the lines, which indicate substantial deviations from the local thermodynamic equilibrium. The interpretation of the spectra thus requires the knowledge of the rate coefficients for the hyperfine excitation of NH<sub>3</sub> induced by collisions with H<sub>2</sub> molecules, the dominant collider in the cold interstellar medium. In this paper, we present the first such calculations using a recoupling approach. The rate coefficients are obtained for all hyperfine levels within rotation–inversion levels up to  $j = 4$  and temperatures up to 100 K by means of quantum scattering close-coupling calculations on an accurate, five-dimensional, potential energy surface. We show that the rate coefficients depart significantly from those obtained with the statistical approach and that they do not conform to any simple propensity rules. Finally, we perform radiative transfer calculations to illustrate the impact of our new rate coefficients by modelling the hyperfine line intensities of the inversion transition in ground-state *para*-NH<sub>3</sub> ( $j_k = 1_1$ ) and of the rotational transition  $1_0 \rightarrow 0_0$  in *ortho*-NH<sub>3</sub>.

**Key words:** molecular data – molecular processes – radiative transfer – scattering – ISM: abundances – ISM: molecules.

## 1 INTRODUCTION

Since its first detection in the interstellar medium (Cheung et al. 1968), ammonia (NH<sub>3</sub>) has often been used to probe the physical properties of molecular clouds due to the favourable structure of its energy levels and its high abundance in a variety of astrophysical sources. The rotational levels of NH<sub>3</sub> are denoted as  $j_k$  (where  $j$  is the angular momentum and  $k$  its projection on the molecular axis), and the presence of metastable states for  $j = k$  that can only decay through molecular collisions makes NH<sub>3</sub> an excellent probe of the local temperature. NH<sub>3</sub> exists in two forms, namely *ortho*-NH<sub>3</sub> (for  $k = 3n$ , where  $n$  is an integer) and *para*-NH<sub>3</sub> (for  $k = 3n \pm 1$ ) that cannot be interconverted through radiative or inelastic collisional processes. In addition, the inversion (or umbrella) motion causes a splitting of each  $j_k$  level into a doublet (with the exception of  $k = 0$  due to spin statistics) whose components, denoted as  $j_k^+$  and  $j_k^-$ , are separated by  $0.79 \text{ cm}^{-1}$  (23.68 GHz). NH<sub>3</sub> can thus be detected in different frequency ranges corresponding to pure inversion, rotational, or vibrational transitions.

In most astrophysical observations, the hyperfine structure due to the electric quadrupole moment of nitrogen is resolved. Nitrogen nuclei possess a spin of  $I = 1$ , so that each rotation–inversion level is further split into three hyperfine components  $F$  (with the exception of ground-state *ortho*-NH<sub>3</sub>), with a separation of the order of a MHz. A rotational line is thus split into five lines: the main line ( $\Delta F = 0$ ), as well as two inner and two outer satellite lines characterized by

$\Delta F = \pm 1$ . The lines are further split by the spins of the H nuclei, but this interaction is much weaker and will be neglected here.

The relative intensity of hyperfine lines can be used to derive opacities if the various hyperfine components have the same excitation temperature and if the opacity is not too large (Barrett, Ho & Myers 1977; Ho & Townes 1983). However, NH<sub>3</sub> hyperfine-resolved observations commonly display anomalies in the spectra, where the intensities within a pair of satellite lines are not equal. This indicates different excitation temperatures, meaning that the satellite components do not obey the local thermodynamic equilibrium (LTE) assumption in the interstellar medium. Such anomalies were first observed by Matsakis et al. (1977) in source DR21 and subsequently by various authors (see e.g. Matsakis et al. 1980; Gaume, Wilson & Johnston 1996; Rathborne et al. 2008; Rosolowsky et al. 2008; Camarata, Jackson & Chambers 2015; Caselli et al. 2017; Zhou et al. 2020) in diverse sources. If the hyperfine levels are not populated thermally, the interpretation of observations requires radiative transfer models to account for non-LTE effects. These occur mainly because of collisional excitation by H<sub>2</sub> molecules, and a knowledge of accurate rate coefficients for the hyperfine excitation of NH<sub>3</sub> by H<sub>2</sub> is thus necessary. In addition, modelling the strength of the hyperfine anomalies can be used to deduce the local H<sub>2</sub> density.

Models to interpret anomalies were developed by Stutzki & Winnewisser (1985a, b) based on rate coefficients calculated for NH<sub>3</sub>–He collisions as a proxy for NH<sub>3</sub>–H<sub>2</sub> collisions. Beside this work, Chen et al. (1998) also computed hyperfine-resolved rate coefficients for NH<sub>3</sub>–He collisions. To this day, there are thus no accurate collisional data for the hyperfine excitation of NH<sub>3</sub> by H<sub>2</sub> molecules.

\* E-mail: jerome.loreau@kuleuven.be

Various theoretical techniques exist to compute such rate coefficients. Among these, the simplest is the statistical approach, which assumes that the rate coefficients for hyperfine excitation are proportional to the hyperfine degeneracy of the final state. In this case, rate coefficients for pure rotational transitions, which are available for molecules such as NH<sub>3</sub>, are the only ingredient needed to obtain hyperfine-resolved rate coefficients. This method was used to interpret the observations of Caselli et al. (2017) for the 1<sub>0</sub>–0<sub>0</sub> transition in the pre-stellar core L1544. The infinite-order sudden (IOS) limit approximation, used by Stutzki & Winnewisser (1985a), ignores the rotational energy spacing and allows again to obtain the hyperfine-resolved rate coefficients on the basis of the pure rotational ones. Given the nature of its assumptions, this approximation is, however, not expected to be valid at low temperatures, i.e. at temperatures close to or lower than the rotational spacings. Finally, the method used in this work is the recoupling approach, which was also adopted by Chen et al. (1998) but for NH<sub>3</sub>–He collisions and combined with the coupled-states approximation.<sup>1</sup> The only approximation in our version of the recoupling approach is the assumption that the hyperfine levels are degenerate, i.e. their splitting is negligible compared to the temperature (Alexander & Dagdigan 1985). While computationally more demanding, it is also expected to be more accurate than the statistical or sudden methods. A summary and comparison of these different approaches can be found in Faure & Lique (2012) for the linear molecules CN and HCN.

In this work, we present rate coefficients for the hyperfine excitation of *ortho*- and *para*-NH<sub>3</sub> in collisions with *para*-H<sub>2</sub> for all levels up to  $j = 4$  and for temperatures up to 100 K. While the rotation–inversion collisional excitation of NH<sub>3</sub> by H<sub>2</sub> has been widely studied theoretically over the past decades (Danby et al. 1987; Offer & Flower 1990; Maret et al. 2009; Ma et al. 2015; Bouhafs et al. 2017; Demes et al. 2023) and experimentally with crossed beams (Schleipen & ter Meulen 1991; Tkac et al. 2015; Gao et al. 2019), to the best of our knowledge this represents the first effort to provide hyperfine collisional excitation rate coefficients of NH<sub>3</sub> (or any non-linear molecule) by H<sub>2</sub> with the accurate recoupling approach.

The paper is structured as follows: in Section 2, we discuss the theoretical methods employed. In Section 3, we discuss the features of the hyperfine-resolved rate coefficients, and in Section 4 we present radiative transfer calculations to investigate the impact of these new data on the modelling of ammonia spectra. Finally, we summarize our findings in Section 5.

## 2 THEORY

The scattering calculations were performed in two steps. First, we computed the scattering matrix for rotation–inversion transitions by means of the fully quantum-mechanical close-coupling (CC) method. This method has been used to obtain accurate cross-sections for rotational excitation of NH<sub>3</sub> induced by collisions with H<sub>2</sub> by several authors (see e.g. Danby et al. 1987; Rist, Alexander & Valiron 1993) and we refer to these papers for further methodological details. Similarly to recent theoretical works (Ma et al. 2015; Bouhafs et al. 2017; Demes et al. 2023), we employ the accurate five-dimensional rigid-rotor potential energy surface of Maret et al. (2009), which was constructed by fitting *ab initio* energies obtained with the

<sup>1</sup>We note that the results of Chen et al. (1998) are questionable and should not be used because some of their rate coefficients are unphysically large (up to 10<sup>−7</sup> cm<sup>3</sup> s<sup>−1</sup>).

coupled cluster method with single, double, and perturbative triple excitations.

The cross-sections for rotation–inversion transitions can be obtained from the  $T$ -matrix elements  $T_{j_1 k v j_2 j_{12} l, j_1' k' v' j_2' j_{12}' l'}$ , where  $v$  denoted the inversion level,  $J$  is the quantum number associated with the total angular momentum of the collision complex without nuclear spin ( $\mathbf{J} = \mathbf{j}_{12} + \mathbf{L}$ ),  $\mathbf{j}_{12} = \mathbf{j}_1 + \mathbf{j}_2$ , where  $\mathbf{j}_1$  and  $\mathbf{j}_2$  are the angular momenta of NH<sub>3</sub> and H<sub>2</sub>, respectively, and  $\mathbf{L}$  is the relative orbital angular momentum of the collision. We do not discuss here the properties of the cross-sections for rotation–inversion transitions as these are identical to those reported recently by Bouhafs et al. (2017) and Demes et al. (2023).

In a second step, the recoupling approach is used to compute hyperfine-resolved cross-sections. When the nuclear spin of the N atom ( $I = 1$ ) is included, each level of NH<sub>3</sub> is split into three components, and the total angular momentum  $\mathbf{J}_t$  is obtained by the coupling  $\mathbf{J}_t = \mathbf{J} + \mathbf{I}$ . However, the hyperfine splittings are of the order of the MHz (i.e. about 10<sup>−5</sup> to 10<sup>−4</sup> K), which is much smaller than the rotational spacings and collisional energies considered here. We thus assume that the hyperfine levels of NH<sub>3</sub> are degenerate. In this case, the nuclear spin wavefunctions can be decoupled from the rotational wavefunctions and, as shown by Offer, van Hemert & van Dishoeck (1994), the angular momenta can also be recoupled as  $\mathbf{F} = \mathbf{j}_1 + \mathbf{I}$ ,  $\mathbf{j}_R = \mathbf{j}_2 + \mathbf{L}$ , and  $\mathbf{J}_t = \mathbf{j}_R + \mathbf{F}$ . The  $T$ -matrix elements including nuclear spin,  $T^{J_t}$ , can then be obtained from the spin-free  $T$ -matrix elements  $T^J$  as

$$T_{j_1 v F j_2 j_{Rl}, j_1' v' F' j_2' j_{Rl}'}^{J_t} = \sum_{J, j_{12}, j_{12}'} (-1)^{j_R + j_R' + l + l' + j_2 + j_2'} ([F][F']][j_{12}][j_{12}'] [j_R][j_R']^{1/2} [J] \left\{ \begin{matrix} j_1 & j_2 & j_{12} \\ l & J & j_R \end{matrix} \right\} \left\{ \begin{matrix} j_1' & j_2' & j_{12}' \\ l' & J & j_R' \end{matrix} \right\} \left\{ \begin{matrix} j_R & j_1 & J \\ I & J_t & F \end{matrix} \right\} \left\{ \begin{matrix} j_R' & j_1' & J \\ I & J_t & F' \end{matrix} \right\} T_{j_1 k v j_2 j_{12} l, j_1' k' v' j_2' j_{12}' l'}^J \quad (1)$$

where  $\{ \dots \}$  denotes a 6- $j$  symbol and  $[x] = 2x + 1$ .

The state-to-state hyperfine cross-sections for NH<sub>3</sub>–H<sub>2</sub> can be then computed from the  $T$ -matrix according to the expression (Offer et al. 1994)

$$\sigma_{j_1 k v F j_2, j_1' k' v' F' j_2'} = \frac{\pi}{k_i^2 (2F + 1)(2j_2 + 1)} \sum_{J_T} (2J_T + 1) \sum_{l' j_R j_R'} |T_{j_1 k v F j_2 j_{Rl}, j_1' k' v' F' j_2' j_{Rl}'}^{J_t}|^2 \quad (2)$$

The scattering calculations were carried out with the HIBRIDON programme (Alexander et al. 2023) for total energies between 0 and 600 cm<sup>−1</sup> on a grid of 700 energies for *ortho*-NH<sub>3</sub> and 660 energies for *para*-NH<sub>3</sub>. These calculations were performed independently for *ortho*-NH<sub>3</sub> and *para*-NH<sub>3</sub> as *ortho*–*para* conversion is forbidden in inelastic collisions. The energy step was 0.5 cm<sup>−1</sup> at the lowest energies and increased gradually up to 4 cm<sup>−1</sup> at the highest energies. We used the log-derivative propagator in the short range, and the Airy propagator in the long range ( $R > 25a_0$ ). Transitions between levels up to  $j_1 = 6$  with  $j_2 = 0$  were converged with a rotational basis including all levels up to  $j_1 = 8$  and  $j_2 = 0, 2$ . The rotational constants of NH<sub>3</sub> were taken as  $A = B = 9.9402$  cm<sup>−1</sup>,  $C = 6.3044$  cm<sup>−1</sup> with an inversion splitting of 0.7903 cm<sup>−1</sup>, while the rotational constant of H<sub>2</sub> was taken as 59.3801 cm<sup>−1</sup> as in Bouhafs et al. (2017). Tests were performed to ensure convergence of the cross-sections with respect to  $J_t$  in equation (2) at all energies, as well with respect to the parameters of the radial grid.

Rate coefficients were then calculated by averaging cross-sections for initial and final states  $i$  and  $f$ ,  $\sigma_{i,f}(E_c)$ , over the Maxwell-Boltzmann distribution of collision energies as expressed:

$$k_{i,f}(T) = \left( \frac{8}{\pi \mu \beta} \right)^{\frac{1}{2}} \beta^2 \int_0^{\infty} E_c \sigma_{i,f}(E_c) e^{-\beta E_c} dE_c. \quad (3)$$

where  $\beta = \frac{1}{k_B T}$  and  $k_B$ ,  $T$ , and  $\mu$  denote the Boltzmann constant, the kinetic temperature, and the NH<sub>3</sub>-H<sub>2</sub> reduced mass, respectively.

### 3 HYPERFINE RATE COEFFICIENTS

Hyperfine excitation rate coefficients were calculated for temperatures up to 100 K and for transitions involving all levels up to  $j_1 = 4$  for both *ortho*-NH<sub>3</sub> and *para*-NH<sub>3</sub>, corresponding to a total of 625 transitions for *ortho*-NH<sub>3</sub> and 2304 transitions for *para*-NH<sub>3</sub>. Only excitation due to  $p$ -H<sub>2</sub> ( $j_2 = 0$ ) is considered here since excited H<sub>2</sub> levels are not significantly populated at the temperatures of molecular clouds where the hyperfine structure is resolved.

Rate coefficients for hyperfine transitions from the rotational state  $2_1^+$  down to level  $1_1^-$  are presented in Fig. 1 as a function of temperature up to 100 K. The rate coefficients are seen to be weakly dependent on  $T$ , a trend that follows directly from the behaviour of the rate coefficients for pure rotational transitions. On the same figure, we also present for comparison the statistical hyperfine rate coefficients. The statistical approach, also known as the  $M_J$  randomizing limit

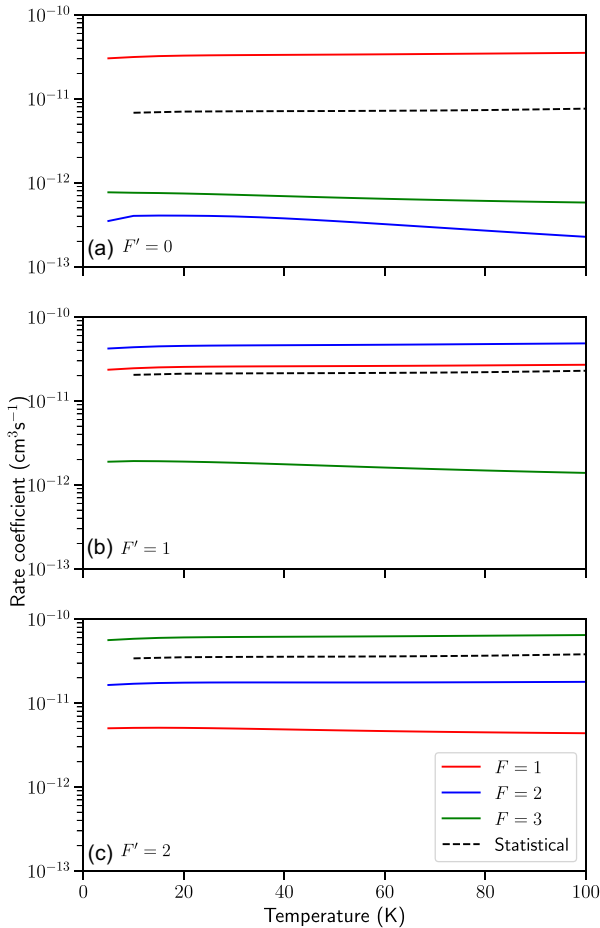


**Figure 1.** Rate coefficients for the transitions  $2_1^+ F \rightarrow 1_1^- F'$  of NH<sub>3</sub> induced by collisions with H<sub>2</sub> as a function of temperature: (a)  $F' = 0$ , (b)  $F' = 1$ , (c)  $F' = 2$ , and comparison to the statistical rate coefficients given by equation (4).

**Table 1.** Rate coefficients for the transitions  $2_1^+ F \rightarrow 1_1^+ F'$  and  $2_1^+ F \rightarrow 1_1^- F'$  of NH<sub>3</sub> induced by H<sub>2</sub> at a temperature of 30 K. Brackets indicate powers of 10.

$j_k v - j'_k v'$		$F' = 0$	$F' = 1$	$F' = 2$
$2_1^+ - 1_1^+$	$F = 1$	5.16[-13]	1.98[-11]	7.27[-12]
	$F = 2$	8.62[-12]	3.11[-12]	1.58[-11]
	$F = 3$	1.85[-13]	8.99[-12]	1.84[-11]
$2_1^+ - 1_1^-$	$F = 1$	3.31[-11]	2.57[-11]	4.97[-12]
	$F = 2$	3.96[-13]	4.58[-11]	1.76[-11]
	$F = 3$	7.19[-13]	1.83[-12]	6.12[-11]

**Table 2.** Quasi-elastic rate coefficients for the excitation  $j_k v F \rightarrow j'_k v' F'$  for rotational levels  $1_1$ ,  $2_2$ , and  $2_1$  of NH<sub>3</sub> by H<sub>2</sub> at 25 K. Comparison with the data of Stutzki & Winnewisser (1985a, last column). Brackets indicate powers of 10.

$j_k$	$F - F'$	$v = -, v' = -$	$v = -, v' = +$	Ref.
$1_1$	0-2	2.43[-11]	1.22[-11]	2.49[-11]
$1_1$	0-1	1.83[-11]	8.96[-11]	8.66[-11]
$1_1$	2-1	1.55[-11]	2.79[-11]	3.28[-11]
$2_2$	1-3	2.58[-12]	1.42[-12]	1.92[-11]
$2_2$	1-2	1.44[-11]	3.05[-11]	7.02[-11]
$2_2$	3-2	7.42[-12]	1.41[-11]	3.88[-11]
$2_1$	2-3	5.31[-12]	8.29[-12]	5.26[-11]
$2_1$	2-1	4.13[-12]	6.84[-12]	4.14[-11]
$2_1$	3-1	7.93[-13]	9.17[-13]	7.41[-12]

(Alexander & Dagdigan 1985), is a commonly used approximation to compute hyperfine-resolved excitation rate coefficients, which assumes that the cross-sections or rate coefficient for hyperfine excitation are directly proportional to the degeneracy of the final hyperfine state and independent of the initial hyperfine state. For NH<sub>3</sub>-H<sub>2</sub>, the statistical rate coefficients are expressed as

$$k_{j_k v F, j'_k v' F'}^{\text{stat}} = \frac{2F' + 1}{(2I + 1)(2j' + 1)} k_{j_k v, j'_k v'}, \quad (4)$$

where  $k_{j_k v, j'_k v'}$  are the nuclear spin-free rate coefficients calculated with the CC method and  $I = 1$ . To simplify the notation, in the remainder of the paper, we use  $j$  to denote the rotational quantum number of NH<sub>3</sub> instead of  $j_1$  without ambiguity since  $j_2 = 0$ .

As can be seen from Fig. 1, for all three final hyperfine states of the transition  $2_1^+ F \rightarrow 1_1^- F'$  the statistical rate coefficients fall between the recoupling values, but a strong dependence on  $F'$  can be observed and large deviations from the  $M_J$  randomizing limit are seen to occur. It is thus clear that the statistical method cannot be used to obtain accurate hyperfine rate coefficients in the case of NH<sub>3</sub>-H<sub>2</sub> collisions.

From Fig. 1, it can be seen that the known propensity rule  $\Delta F = \Delta j$  (Alexander & Dagdigan 1985) holds for the transitions within  $2_1^+ \rightarrow 1_1^-$ . However, this is not a general trend. In Table 1, we report the rate coefficients for transitions from levels  $2_1^+ F$  down to levels  $1_1^+ F$  and  $1_1^- F$  at a fixed temperature of 30 K. For the case of  $2_1^+ F$  to  $1_1^+ F$  transitions (as well as for a large number of transitions involving higher lying rotational levels), the  $\Delta F = \Delta j$  propensity rule is not respected. In addition, Table 1 also shows that the largest rate coefficients are not necessarily those with the largest  $F'$ , as would be expected from a statistical behaviour.

Of interest are also the quasi-elastic rate coefficients, i.e. rate coefficients for hyperfine excitation within a single rotational level. We present in Table 2 the quasi-elastic rate coefficients  $j_k v F \rightarrow$

**Table 3.** Relative factors (equation 5) for the transitions  $1_1^+ F \rightarrow 2_1^+ F'$  and  $1_1^+ F \rightarrow 2_1^- F'$  of  $\text{NH}_3$  induced by  $\text{H}_2$  at a temperature of 25 K. The values in parentheses are from Stutzki & Winnewisser (1985a).

		$F' = 1$	$F' = 2$	$F' = 3$
$1_1^+ F - 2_1^+ F'$	$F = 0$	0.03 (0.08)	0.95 (0.65)	0.02 (0.27)
	$F = 1$	0.43 (0.31)	0.11 (0.20)	0.46 (0.48)
	$F = 2$	0.09 (0.16)	0.35 (0.35)	0.56 (0.50)
$1_1^+ F - 2_1^- F'$	$F = 0$	0.93 (0.57)	0.02 (0.28)	0.05 (0.15)
	$F = 1$	0.24 (0.27)	0.72 (0.50)	0.04 (0.23)
	$F = 2$	0.03 (0.09)	0.17 (0.24)	0.81 (0.67)

$j_k v F'$  at 25 K for the first three rotational states of *para*- $\text{NH}_3$ , and for the antisymmetric inversion level ( $v = v' = -$ ). The corresponding  $F-F'$  transitions involving the symmetric inversion levels ( $v = v' = +$ ) are similar although not identical, with differences of up to a few percent (not shown). In addition, we also report in the same table the rate coefficients corresponding to a change of inversion level ( $- \rightarrow +$ ; the reverse rate coefficients can be obtained by detailed balance). It should be noted that those are not strictly quasi-elastic, since the  $- \rightarrow +$  pure inversion transition corresponds to an energy transfer of  $0.79 \text{ cm}^{-1}$ . It can be noticed that the rate coefficients strongly depend on the final inversion level, with differences that reach a factor 5 between  $v' = -$  and  $v' = +$ . Interestingly, the rate coefficients for inversion-conserving transitions  $j_k^- F \rightarrow j_k^- F'$ , which would be elastic if the nuclear spin were neglected, are in many cases smaller than those of the corresponding inversion-changing transitions  $j_k^- F \rightarrow j_k^+ F'$ . Finally, the last column of Table 2 compares our values to the results of Stutzki & Winnewisser (1985a), which are independent of the inversion level, and show important discrepancies of up to an order of magnitude for some quasi-elastic transitions. It is worth emphasizing that those results were obtained using a different method, namely the IOS approximation, which is not expected to be accurate at low temperatures. In addition, Stutzki & Winnewisser (1985a) used a potential for  $\text{NH}_3\text{-He}$  instead of  $\text{NH}_3\text{-H}_2$ , which leads to an additional error. Finally, we note that our quasi-elastic rate coefficients are of the same order of magnitude as those for inelastic transitions.

From their IOS calculations, Stutzki & Winnewisser (1985a) compute relative factors, defined as the ratio of hyperfine rate coefficients divided by the rotational excitation rate coefficient,

$$g_{FF'} = \frac{k_{j_k v F, j' k' v' F'}}{k_{j_k v, j' k' v'}}. \quad (5)$$

While the absolute IOS rate coefficients are not expected to be accurate at low temperature, the method should provide relative factors that are better than the statistical ones. These relative factors obtained with the recoupling approach are presented in Table 3 and compared to the IOS results of Stutzki & Winnewisser (1985a) for the  $1_1^+ - 2_1^+$  and  $1_1^+ - 2_1^-$  excitation transitions. We observe that in most cases the IOS method does predict the correct propensities, and performs better than the statistical approach, as expected. On the other hand, it is clear that IOS is not sufficient to obtain accurate rate coefficients, since discrepancies of up to 50 per cent are seen for the dominant rate coefficients and up to a factor 10 for the smallest rate coefficients. Moreover, both the IOS and recoupling relative factors are almost independent of the temperature in the range explored here (see Fig. 1), which shows that the discrepancies discussed above remain up to temperatures of at least 100 K.

## 4 RADIATIVE TRANSFER CALCULATIONS

In order to investigate the impact of the hyperfine rate coefficients on the non-LTE modelling of  $\text{NH}_3$  spectra, we present below simple radiative transfer calculations using two different sets of hyperfine-resolved collisional data: (1) the precise set of *recoupling* rate coefficients and (2) the approximate set of *statistical* rate coefficients, as defined in equation (4).

Radiative transfer calculations were performed with the non-LTE RADEX programme (van der Tak et al. 2007) using the large velocity gradient formalism for an expanding sphere. The code was employed to compute the radiation temperature  $T_R$  of low-lying hyperfine transitions in both *para*- and *ortho*- $\text{NH}_3$ . The hyperfine energy levels and radiative rates were taken from the CDMS catalogue (Müller et al. 2005). The kinetic temperature was fixed at 10 K, which is typical of cold molecular clouds, while the hydrogen density was varied in the range  $10^2\text{--}10^9 \text{ cm}^{-3}$ . The *para*- $\text{NH}_3$  (or *ortho*- $\text{NH}_3$ ) column densities were selected in the range  $10^{12}\text{--}10^{15} \text{ cm}^{-2}$  with a line width (full width at half-maximum) of  $1 \text{ km s}^{-1}$ . No radiation field was considered except the cosmic microwave background at 2.73 K. We have also checked with the MOLPOP code (Asensio Ramos & Elitzur 2018) that line overlap effects, which are ignored by RADEX, are mostly negligible with the above parameters, allowing us to focus on the impact of the collisional data.

We first consider the inversion transition  $1_1^- \rightarrow 1_1^+$  of *para*- $\text{NH}_3$  at 23.68 GHz. This transition has been widely observed in the interstellar medium since its first detection by Cheung et al. (1968). Anomalies in the hyperfine intensities of this line were reported in the 1970s (Matsakis et al. 1977) and these anomalies are now known to be very common in star-forming regions. In the anomalous spectra, the intensities of the outer satellite lines are not equal: the  $F = 0 \rightarrow 1$  component is stronger and the  $F = 1 \rightarrow 0$  component is weaker than expected. Radiative transfer models have shown that these anomalies can be reproduced by non-LTE effects induced by photon trapping of selected hyperfine transitions in the rotational transition  $2_1^{+/-} \rightarrow 1_1^{-/+}$ , as explained by Stutzki & Winnewisser (1985b; see, in particular, their fig. 2). Systematic motions, such as expansion and collapse, are also expected to play a role and the relative contribution of these effects remains a matter of debate (see Zhou et al. 2020, and references therein). In any case, because non-LTE populations depend on the competition between the radiative and collisional rates, the accuracy of hyperfine selective collisional rate coefficients should be critical for a correct interpretation of the anomalies in the  $1_1^- \rightarrow 1_1^+$  inversion transition.

In Fig. 2, we have plotted the intensity ratio of the outer hyperfine satellite line  $F = 0 \rightarrow 1$  relative to the strongest component  $F = 2 \rightarrow 2$ , for the two sets of collisional rates (recoupling and statistical). At low hydrogen density, the ratio is found to increase above the ‘natural’ intensity ratio (0.266) as soon as the column density exceeds  $\sim 10^{14} \text{ cm}^{-2}$ . The ratios then increase with increasing density and plateau are reached when  $n(\text{H}_2)$  is larger than about  $10^5 \text{ cm}^{-3}$ , where LTE conditions are fulfilled. For column densities above  $\sim 10^{14} \text{ cm}^{-2}$ , we can notice the impact of the collisional data set: the intensity ratios are decreased by up to 20 per cent when the statistical data set is employed. This demonstrates the importance of the hyperfine propensity rules when the total opacity of the line is larger than  $\sim 1$ . A similar result was actually observed by Stutzki & Winnewisser (1985a) using hyperfine collision rates computed with the IOS approximation and using helium instead of  $\text{H}_2$  as the collider. As concluded by these authors, a precise knowledge of the hyperfine-resolved rate coefficients is thus required for a reliable modelling of observational data.

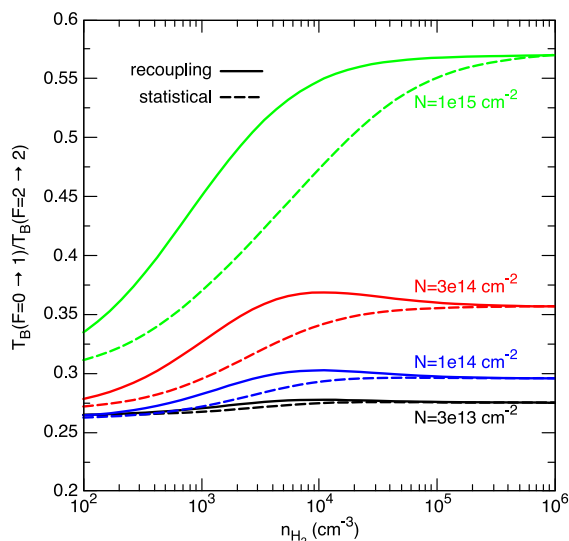


**Figure 2.** The intensity ratio of the hyperfine satellite line  $F = 0 \rightarrow 1$  of the *para*- $\text{NH}_3$   $j_k = 1_1$  inversion transition relative to the strongest component  $F = 2 \rightarrow 2$  as a function of the hydrogen density for a set of column densities. The kinetic temperature is fixed at 10 K and the line width at  $1 \text{ km s}^{-1}$ .

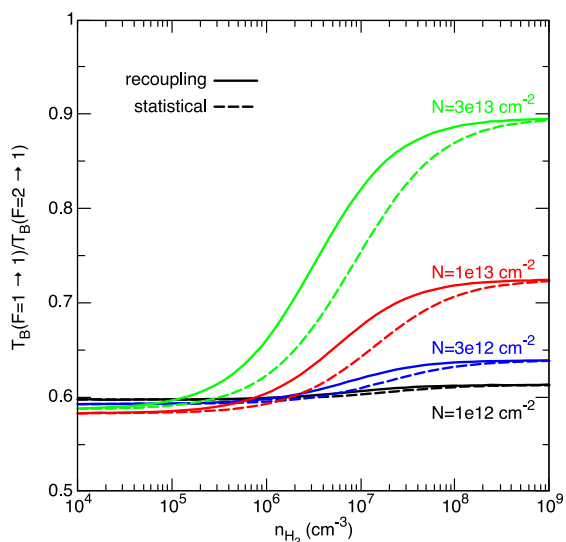


**Figure 3.** The intensity ratio of the hyperfine component  $F = 1 \rightarrow 1$  of the *ortho*- $\text{NH}_3$   $j_k = 1_0 \rightarrow 0_0$  rotational transition relative to the strongest component  $F = 2 \rightarrow 1$  as a function of the hydrogen density for a set of column densities. The kinetic temperature is fixed at 10 K and the line width at  $1 \text{ km s}^{-1}$ .

A second example is the *ortho*- $\text{NH}_3$  ground-state rotational transition  $1_0^+ \rightarrow 0_0^-$  at 572.5 GHz. The electric quadrupole hyperfine structure of this line was resolved for the first time in space thanks to *Herschel* observations towards the cold pre-stellar core L1544 (Caselli et al. 2017). The three hyperfine components were found to be heavily self-absorbed and a sophisticated radiative transfer model was employed to reproduce the observed profile and to deduce the  $\text{NH}_3$  radial abundance in the core. In that work, hyperfine selective collisional data were generated from the rotational rate coefficients of Bouhafs et al. (2017) by applying the statistical approach to the electric quadrupole and magnetic hyperfine splittings. In Fig. 3, we have plotted the intensity ratio of the hyperfine component  $F = 1 \rightarrow 1$  relative to the strongest component  $F = 2 \rightarrow 1$ , again for the

two sets of collisional rates (recoupling and statistical). We note that our statistical set is identical to that used by Caselli et al. (2017) except that the magnetic splittings ( $< 100 \text{ kHz}$ ) are neglected here. At low hydrogen density, the ratio is found to lie slightly below the natural intensity ratio (0.6) for column density above  $\sim 10^{12} \text{ cm}^{-2}$ . When the  $\text{H}_2$  density exceeds  $\sim 10^5 \text{ cm}^{-3}$ , however, the intensity ratios rise above 0.6 and the LTE plateaus are reached at  $\text{H}_2$  densities larger than  $\sim 10^8 \text{ cm}^{-3}$ , as expected from the large radiative rates ( $A \sim 1.58 \times 10^{-3}$ ). The impact of the rate coefficients is smaller than in the case of the *para*- $\text{NH}_3$  transition (Fig. 2) with a maximum difference of  $\sim 10$  per cent in the intensity ratios. This is not really surprising since the recoupling and statistical rate coefficients for the hyperfine transitions  $1_0^+ F \rightarrow 0_0^- F' = 1$  are identical and equal to the pure rotational rate coefficients (by construction since the rotational  $0_0^-$  level has a single hyperfine sub-level  $F = 1$ ). Thus, only the rate coefficients corresponding to hyperfine transitions within the rotational level  $1_0^+$ , the so-called quasi-elastic rate coefficients, are different in the two data sets: they are set to zero in the statistical set, while they are comparable to the pure rotational rate coefficient in the recoupling set. We can conclude that the quasi-elastic rate coefficients have a significant although moderate impact in the radiative transfer calculation.

Finally, we wish to stress that the above results are only illustrative: more sophisticated radiative transfer calculations are clearly needed to explore a much larger parameter space and to include line overlap as well as systematic motion effects. Preliminary calculations with MOLPOP show, for instance, that for kinetic temperatures larger than 10 K and column densities above  $10^{15} \text{ cm}^{-3}$ , line overlap effects can increase the intensity ratio  $F = 0 \rightarrow 1/F = 2 \rightarrow 2$  in the  $1_1^- - 1_1^+$  inversion transition by more than 50 per cent. The combination of the present recoupling rate coefficients with one-dimensional radiative transfer codes able to handle hyperfine overlaps, such as ALICO (Magalhães et al. 2018), will be particularly valuable to revisit the  $\text{NH}_3$  hyperfine anomalies and to more firmly establish the role of non-LTE effects.

## 5 CONCLUSION

We have presented a full set of rate coefficients for the hyperfine excitation of *ortho*- and *para*- $\text{NH}_3$  in collisions with *para*- $\text{H}_2$  for all levels of  $\text{NH}_3$  up to  $j = 4$  and for temperatures up to 100 K. The calculations were performed by means of the accurate recoupling technique, which relies on quantum-mechanical CC scattering calculations. In general, the rate coefficients are weakly dependent on the temperature, but depend strongly on all quantum numbers of  $\text{NH}_3$ . We found no clear propensity rules, and a comparison with statistical rate coefficients (which are independent of the initial hyperfine level) showed important deviations from this approximation. In addition, we also found large differences with previously published results on  $\text{NH}_3$ -He collisions.

Using a simple non-LTE model, we illustrated the difference between the accurate recoupling rate coefficients and the approximate statistical rate coefficients on the inversion transition in ground-state *para*- $\text{NH}_3$  ( $1_1^- F \rightarrow 1_1^+ F'$ ) at 23.68 GHz and on the rotational transition  $1_0^+ F \rightarrow 0_0^- F'$  in *ortho*- $\text{NH}_3$ . These simple calculations demonstrate that the two sets of rate coefficients lead to significant differences. Moreover, non-LTE effects are predicted for column density in excess of  $\sim 10^{12} \text{ cm}^{-2}$ . An important extension of this work will be to perform radiative transfer calculations using a model that can treat line overlaps that play a key role in  $\text{NH}_3$  hyperfine anomalies. This would allow the investigation of non-LTE effects at

higher temperatures, thus involving higher lying rotational states of ammonia.

As a reminder, the present calculations only considered the hyperfine splitting due to the nitrogen nucleus but did not take into account the (much smaller) further hyperfine magnetic splitting due to the three protons, which is sometimes resolved in astronomical spectra (Rydbeck et al. 1977). We suggest that the corresponding rate coefficients can be obtained from those presented here using the statistical approximation.

Finally, it should also be noted that the recoupling calculations presented in this work are accurate but computationally expensive. At the other end, statistical rate coefficients can be immediately obtained provided the rate coefficients for pure rotational excitation are available. An intermediate approach is the IOS method, which has been used with some success for the hyperfine excitation of linear molecules by H<sub>2</sub> (Goicoechea, Lique & Santa-Maria 2022). Extending the IOS method and recoupling theory to asymmetric polyatomic molecules would be beneficial in order to generate sets of hyperfine-resolved rate coefficients for other molecules such as deuterated ammonia (NH<sub>2</sub>D, NHD<sub>2</sub>) or H<sub>2</sub>CO.

## ACKNOWLEDGEMENTS

Brian Svoboda is acknowledged for useful discussions. JL acknowledges support from KU Leuven through grant no. 19-00313. Moreover, we acknowledge financial support from the European Research Council (Consolidator Grant COLLEXISM, grant agreement no. 811363). FL acknowledges financial support from the Institut Universitaire de France and the Programme National ‘Physique et Chimie du Milieu Interstellaire’ (PCMI) of CNRS/INSU with INC/INP cofunded by CEA and CNES.

## DATA AVAILABILITY

The data underlying this article are available as supplementary material to the article and the full set of rate coefficients will be made available through the EMAA data base (<https://emaa.osug.fr> and <https://dx.doi.org/10.17178/EMAA>).

## REFERENCES

- Alexander M. H., Dagdigian P. J., 1985, *J. Chem. Phys.*, 83, 2191  
 Alexander M., Dagdigian P., Werner H.-J., Klos J., Desrousseaux B., Raffy G., Lique F., 2023, *Comput. Phys. Commun.*, 289, 108761  
 Asensio Ramos A., Elitzur M., 2018, *A&A*, 616, A131  
 Barrett A. H., Ho P. T. P., Myers P. C., 1977, *ApJ*, 211, L39  
 Bouhafs N., Rist C., Daniel F., Dumouchel F., Lique F., Wiesenfeld L., Faure A., 2017, *MNRAS*, 470, 2204  
 Camarata M. A., Jackson J. M., Chambers E., 2015, *ApJ*, 806, 74  
 Caselli P. et al., 2017, *A&A*, 603, L1

- Chen J., hui Zhang Y., Zeng Q., Pei C.-C., 1998, *J. Phys. B: Atom. Mol. Opt. Phys.*, 31, 1259  
 Cheung A. C., Rank D. M., Townes C. H., Thornton D. D., Welch W. J., 1968, *Phys. Rev. Lett.*, 21, 1701  
 Danby G., Flower D. R., Valiron P., Kochanski E., Kurdi L., Diercksen G. H. F., 1987, *J. Phys. B: Atom. Mol. Phys.*, 20, 1039  
 Demes S., Lique F., Loreau J., Faure A., 2023, *MNRAS*, 524, 2368  
 Faure A., Lique F., 2012, *MNRAS*, 425, 740  
 Gao Z., Loreau J., van der Avoird A., van de Meerakker S. Y. T., 2019, *Phys. Chem. Chem. Phys.*, 21, 14033  
 Gaume R. A., Wilson T. L., Johnston K. J., 1996, *ApJ*, 457, L47  
 Goicoechea J. R., Lique F., Santa-Maria M. G., 2022, *A&A*, 658, A28  
 Ho P. T. P., Townes C. H., 1983, *ARA&A*, 21, 239  
 Ma Q., van der Avoird A., Loreau J., Alexander M., van de Meerakker S. Y. T., Dagdigian P. J., 2015, *J. Chem. Phys.*, 143, 044312  
 Magalhães V. S., Hily-Blant P., Faure A., Hernandez-Vera M., Lique F., 2018, *A&A*, 615, A52  
 Maret S., Faure A., Scifoni E., Wiesenfeld L., 2009, *MNRAS*, 399, 425  
 Matsakis D. N., Brandshaft D., Chui M. F., Cheung A. C., Yngvesson K. S., Cardiasmenos A. G., Shanley J. F., Ho P. T. P., 1977, *ApJ*, 214, L67  
 Matsakis D. N., Bologna J. M., Schwartz P. R., Cheung A. C., Townes C. H., 1980, *ApJ*, 241, 655  
 Müller H. S. P., Schlöder F., Stutzki J., Winnewisser G., 2005, *J. Mol. Struct.*, 742, 215  
 Offer A., Flower D. R., 1990, *J. Chem. Soc. Faraday Trans.*, 86, 1659  
 Offer A. R., van Hemert M. C., van Dishoeck E. F., 1994, *J. Chem. Phys.*, 100, 362  
 Rathborne J. M., Lada C. J., Muench A. A., Alves J. F., Lombardi M., 2008, *ApJS*, 174, 396  
 Rist C., Alexander M. H., Valiron P., 1993, *J. Chem. Phys.*, 98, 4662  
 Rosolowsky E. W., Pineda J. E., Foster J. B., Borkin M. A., Kauffmann J., Caselli P., Myers P. C., Goodman A. A., 2008, *ApJS*, 175, 509  
 Rydbeck O. E. H., Sume A., Hjalmarson A., Ellder J., Ronnang B. O., Kollberg E., 1977, *ApJ*, 215, L35  
 Schleipen J., ter Meulen J., 1991, *Chem. Phys.*, 156, 479  
 Stutzki J., Winnewisser G., 1985a, *A&A*, 144, 1  
 Stutzki J., Winnewisser G., 1985b, *A&A*, 144, 13  
 Tkac O., Saha A. K., Loreau J., Ma Q., Dagdigian P. J., Parker D. H., van der Avoird A., Orr-Ewing A. J., 2015, *Mol. Phys.*, 113, 3925  
 van der Tak F. F. S., Black J. H., Schöier F. L., Jansen D. J., van Dishoeck E. F., 2007, *A&A*, 468, 627  
 Zhou D.-d., Wu G., Esimbek J., Henkel C., Zhou J.-j., Li D.-l., Ji W.-g., Zheng X.-w., 2020, *A&A*, 640, A114

## SUPPORTING INFORMATION

Supplementary data are available at *MNRAS* online. Please note: Oxford University Press is not responsible for the content or functionality of any supporting materials supplied by the authors. Any queries (other than missing material) should be directed to the corresponding author for the article.

This paper has been typeset from a  $\text{\TeX}/\text{\LaTeX}$  file prepared by the author.

# List of astronomical key words (Updated on 2020 January)

This list is common to *Monthly Notices of the Royal Astronomical Society*, *Astronomy and Astrophysics*, and *The Astrophysical Journal*. In order to ease the search, the key words are subdivided into broad categories. No more than *six* subcategories altogether should be listed for a paper.

The subcategories in boldface containing the word ‘individual’ are intended for use with specific astronomical objects; these should never be used alone, but always in combination with the most common names for the astronomical objects in question. Note that each object counts as one subcategory within the allowed limit of six.

The parts of the key words in italics are for reference only and should be omitted when the keywords are entered on the manuscript.

## **General**

editorials, notices  
errata, addenda  
extraterrestrial intelligence  
history and philosophy of astronomy  
miscellaneous  
obituaries, biographies  
publications, bibliography  
sociology of astronomy  
standards

## **Physical data and processes**

acceleration of particles  
accretion, accretion discs  
asteroseismology  
astrobiology  
astrochemistry  
astroparticle physics  
atomic data  
atomic processes  
black hole physics  
chaos  
conduction  
convection  
dense matter  
diffusion  
dynamo  
elementary particles  
equation of state  
gravitation  
gravitational lensing: micro  
gravitational lensing: strong  
gravitational lensing: weak  
gravitational waves  
hydrodynamics  
instabilities  
line: formation  
line: identification  
line: profiles  
magnetic fields  
magnetic reconnection  
(*magnetohydrodynamics*) MHD  
masers  
molecular data  
molecular processes  
neutrinos  
nuclear reactions, nucleosynthesis, abundances  
opacity  
plasmas  
polarization

radiation: dynamics  
radiation mechanisms: general  
radiation mechanisms: non-thermal  
radiation mechanisms: thermal  
radiative transfer  
relativistic processes  
scattering  
shock waves  
solid state: refractory  
solid state: volatile  
turbulence  
waves

## **Astronomical instrumentation, methods and techniques**

atmospheric effects  
balloons  
instrumentation: adaptive optics  
instrumentation: detectors  
instrumentation: high angular resolution  
instrumentation: interferometers  
instrumentation: miscellaneous  
instrumentation: photometers  
instrumentation: polarimeters  
instrumentation: spectrographs  
light pollution  
methods: analytical  
methods: data analysis  
methods: laboratory: atomic  
methods: laboratory: molecular  
methods: laboratory: solid state  
methods: miscellaneous  
methods: numerical  
methods: observational  
methods: statistical  
site testing  
space vehicles  
space vehicles: instruments  
techniques: high angular resolution  
techniques: image processing  
techniques: imaging spectroscopy  
techniques: interferometric  
techniques: miscellaneous  
techniques: photometric  
techniques: polarimetric  
techniques: radar astronomy  
techniques: radial velocities  
techniques: spectroscopic  
telescopes

## **Astronomical data bases**

astronomical data bases: miscellaneous  
atlases  
catalogues  
surveys  
virtual observatory tools

## **Software**

software: data analysis  
software: development  
software: documentation  
software: public release  
software: simulations

## **Astrometry and celestial mechanics**

astrometry  
celestial mechanics  
eclipses  
ephemerides  
occultations  
parallaxes  
proper motions  
reference systems  
time

## **The Sun**

Sun: abundances  
Sun: activity  
Sun: atmosphere  
Sun: chromosphere  
Sun: corona  
Sun: coronal mass ejections (CMEs)  
Sun: evolution  
Sun: faculae, plages  
Sun: filaments, prominences  
Sun: flares  
Sun: fundamental parameters  
Sun: general  
Sun: granulation  
Sun: helioseismology  
Sun: heliosphere  
Sun: infrared  
Sun: interior  
Sun: magnetic fields  
Sun: oscillations  
Sun: particle emission  
Sun: photosphere  
Sun: radio radiation  
Sun: rotation  
(*Sun:*) solar–terrestrial relations  
(*Sun:*) solar wind  
(*Sun:*) sunspots  
Sun: transition region  
Sun: UV radiation  
Sun: X-rays, gamma-rays

## **Planetary systems**

comets: general

## **comets: individual: . . .**

Earth  
interplanetary medium  
Kuiper belt: general

## **Kuiper belt objects: individual: . . .**

meteorites, meteors, meteoroids

minor planets, asteroids: general

## **minor planets, asteroids: individual: . . .**

Moon  
Oort Cloud  
planets and satellites: atmospheres  
planets and satellites: aurorae  
planets and satellites: composition  
planets and satellites: detection  
planets and satellites: dynamical evolution and stability  
planets and satellites: formation  
planets and satellites: fundamental parameters  
planets and satellites: gaseous planets  
planets and satellites: general

## **planets and satellites: individual: . . .**

planets and satellites: interiors  
planets and satellites: magnetic fields  
planets and satellites: oceans  
planets and satellites: physical evolution  
planets and satellites: rings  
planets and satellites: surfaces  
planets and satellites: tectonics  
planets and satellites: terrestrial planets  
planet–disc interactions  
planet–star interactions  
protoplanetary discs  
zodiacal dust

## **Stars**

stars: abundances  
stars: activity  
stars: AGB and post-AGB  
stars: atmospheres  
(*stars:*) binaries (*including multiple*): close  
(*stars:*) binaries: eclipsing  
(*stars:*) binaries: general  
(*stars:*) binaries: spectroscopic  
(*stars:*) binaries: symbiotic  
(*stars:*) binaries: visual  
stars: black holes  
(*stars:*) blue stragglers  
(*stars:*) brown dwarfs  
stars: carbon  
stars: chemically peculiar  
stars: chromospheres  
(*stars:*) circumstellar matter  
stars: coronae  
stars: distances  
stars: dwarf novae  
stars: early-type  
stars: emission-line, Be  
stars: evolution  
stars: flare  
stars: formation  
stars: fundamental parameters  
(*stars:*) gamma-ray burst: general  
(*stars:*) **gamma-ray burst: individual: . . .**  
stars: general  
(*stars:*) Hertzsprung–Russell and colour–magnitude diagrams  
stars: horizontal branch  
stars: imaging  
**stars: individual: . . .**  
stars: interiors



- stars: jets
- stars: kinematics and dynamics
- stars: late-type
- stars: low-mass
- stars: luminosity function, mass function
- stars: magnetars
- stars: magnetic fields
- stars: massive
- stars: mass-loss
- stars: neutron
- (stars:) novae, cataclysmic variables
- stars: oscillations (*including pulsations*)
- stars: peculiar (*except chemically peculiar*)
- (stars:) planetary systems
- stars: Population II
- stars: Population III
- stars: pre-main-sequence
- stars: protostars
- (stars:) pulsars: general
- (stars:) **pulsars: individual: . . .**
- stars: rotation
- stars: solar-type
- (stars:) starspots
- stars: statistics
- (stars:) subdwarfs
- (stars:) supergiants
- (stars:) supernovae: general
- (stars:) **supernovae: individual: . . .**
- stars: variables: Cepheids
- stars: variables: Scuti
- stars: variables: general
- stars: variables: RR Lyrae
- stars: variables: S Doradus
- stars: variables: T Tauri, Herbig Ae/Be
- (stars:) white dwarfs
- stars: winds, outflows
- stars: Wolf–Rayet

### **Interstellar medium (ISM), nebulae**

- ISM: abundances
- ISM: atoms
- ISM: bubbles
- ISM: clouds
- (ISM:) cosmic rays
- (ISM:) dust, extinction
- ISM: evolution
- ISM: general
- (ISM:) HII regions
- (ISM:) Herbig–Haro objects

### **ISM: individual objects: . . .**

- (*except planetary nebulae*)
- ISM: jets and outflows
- ISM: kinematics and dynamics
- ISM: lines and bands
- ISM: magnetic fields
- ISM: molecules
- (ISM:) photodissociation region (PDR)
- (ISM:) planetary nebulae: general
- (ISM:) **planetary nebulae: individual: . . .**
- ISM: structure
- ISM: supernova remnants

### **The Galaxy**

- Galaxy: abundances
- Galaxy: bulge
- Galaxy: centre
- Galaxy: disc
- Galaxy: evolution
- Galaxy: formation
- Galaxy: fundamental parameters
- Galaxy: general
- (Galaxy:) globular clusters: general
- (Galaxy:) **globular clusters: individual: . . .**
- Galaxy: halo
- Galaxy: kinematics and dynamics
- (Galaxy:) local interstellar matter
- Galaxy: nucleus
- (Galaxy:) open clusters and associations: general
- (Galaxy:) **open clusters and associations: individual: . . .**
- (Galaxy:) solar neighbourhood
- Galaxy: stellar content
- Galaxy: structure

### **Galaxies**

- galaxies: abundances
- galaxies: active
- galaxies: bar
- (galaxies:) BL Lacertae objects: general
- (galaxies:) **BL Lacertae objects: individual: . . .**
- galaxies: bulges
- galaxies: clusters: general

### **galaxies: clusters: individual: . . .**

- galaxies: clusters: intracluster medium
- galaxies: disc
- galaxies: distances and redshifts
- galaxies: dwarf
- galaxies: elliptical and lenticular, cD
- galaxies: evolution
- galaxies: formation
- galaxies: fundamental parameters
- galaxies: general
- galaxies: groups: general

### **galaxies: groups: individual: . . .**

- galaxies: haloes
- galaxies: high-redshift

### **galaxies: individual: . . .**

- galaxies: interactions
- (galaxies:) intergalactic medium
- galaxies: irregular
- galaxies: ISM
- galaxies: jets
- galaxies: kinematics and dynamics
- (galaxies:) Local Group
- galaxies: luminosity function, mass function
- (galaxies:) Magellanic Clouds
- galaxies: magnetic fields
- galaxies: nuclei
- galaxies: peculiar
- galaxies: photometry
- (galaxies:) quasars: absorption lines
- (galaxies:) quasars: emission lines
- (galaxies:) quasars: general

*(galaxies:)* **quasars: individual: . . .**  
*(galaxies:)* quasars: supermassive black holes  
galaxies: Seyfert  
galaxies: spiral  
galaxies: starburst  
galaxies: star clusters: general

**galaxies: star clusters: individual: . . .**  
galaxies: star formation  
galaxies: statistics  
galaxies: stellar content  
galaxies: structure

### **Cosmology**

*(cosmology:)* cosmic background radiation  
*(cosmology:)* cosmological parameters  
*(cosmology:)* dark ages, reionization, first stars  
*(cosmology:)* dark energy  
*(cosmology:)* dark matter  
*(cosmology:)* diffuse radiation  
*(cosmology:)* distance scale  
*(cosmology:)* early Universe  
*(cosmology:)* inflation  
*(cosmology:)* large-scale structure of Universe  
cosmology: miscellaneous  
cosmology: observations  
*(cosmology:)* primordial nucleosynthesis  
cosmology: theory

### **Resolved and unresolved sources as a function of wavelength**

gamma-rays: diffuse background  
gamma-rays: galaxies  
gamma-rays: galaxies: clusters  
gamma-rays: general  
gamma-rays: ISM  
gamma-rays: stars  
infrared: diffuse background  
infrared: galaxies  
infrared: general  
infrared: ISM  
infrared: planetary systems  
infrared: stars  
radio continuum: galaxies  
radio continuum: general  
radio continuum: ISM  
radio continuum: planetary systems  
radio continuum: stars  
radio continuum: transients  
radio lines: galaxies  
radio lines: general  
radio lines: ISM  
radio lines: planetary systems  
radio lines: stars  
submillimetre: diffuse background  
submillimetre: galaxies  
submillimetre: general  
submillimetre: ISM  
submillimetre: planetary systems  
submillimetre: stars  
ultraviolet: galaxies

ultraviolet: general  
ultraviolet: ISM  
ultraviolet: planetary systems  
ultraviolet: stars  
X-rays: binaries  
X-rays: bursts  
X-rays: diffuse background  
X-rays: galaxies  
X-rays: galaxies: clusters  
X-rays: general  
**X-rays: individual: . . .**  
X-rays: ISM  
X-rays: stars

### **Transients**

*(transients:)* black hole mergers  
*(transients:)* black hole - neutron star mergers  
*(transients:)* fast radio bursts  
*(transients:)* gamma-ray bursts  
*(transients:)* neutron star mergers  
transients: novae  
transients: supernovae  
transients: tidal disruption events